



# Measurement of the bubble nucleation temperature of water on a pulse-heated thin platinum film supported by a membrane using a low-noise bridge circuit



Eric J. Ching<sup>a</sup>, C. Thomas Avedisian<sup>a,\*</sup>, Michael J. Carrier<sup>b</sup>, Richard C. Cavicchi<sup>b</sup>, James R. Young<sup>a</sup>, Bruce R. Land<sup>c</sup>

<sup>a</sup> Sibley School of Mechanical and Aerospace Engineering, Cornell University, Ithaca, NY 14853, United States

<sup>b</sup> Biomolecular Measurement Division, National Institute of Standards and Technology, Gaithersburg, MD 20899, United States

<sup>c</sup> School of Electrical and Computer Engineering, Cornell University, Ithaca, NY 14853, United States

## ARTICLE INFO

### Article history:

Received 4 February 2014

Received in revised form 24 July 2014

Accepted 24 July 2014

### Keywords:

Boiling  
Superheat  
Bubble nucleation  
Inkjet  
Bubbles  
Printer  
Microscale  
Bubble pump  
Homogeneous nucleation

## ABSTRACT

This study describes the performance of stress-minimized platinum (Pt) films supported by thin membranes (200 nm thick) to promote bubble nucleation of water near its theoretical superheat limit. The membrane configurations consist of Pt films deposited on 200 nm thick SiN films over bulk Si, with membranes being formed by etching Si from the back side of the films. Results are compared with more conventional Pt films supported by SiO<sub>2</sub> and Si substrates.

The average metal temperature is monitored by a bridge circuit with capacitive and inductive filtering to reduce noise in the output signal. Voltage pulses with durations ranging between 0.5 and 10 μs are imposed on the bridge to electrically heat the Pt film. The paper includes discussion of fabrication of the films, their treatment prior to using them as temperature sensors, the bridge circuit design for monitoring the change in electrical resistance during the power pulse, the calibration process of the films, and results of the bubble nucleation temperatures for the range of pulse durations examined.

The results show that significantly less power is needed to trigger bubble nucleation on a membrane-supported platinum film compared to a platinum film on a bulk Si substrate. The nucleation temperatures which were closest to the theoretical limit of water were realized at heating rates of nearly 10<sup>9</sup> C/s. The potential for employing back-side etched devices is suggested for fundamental studies of phase transitions of highly superheated liquids and in applications where bubble nucleation is an important process such as for ink-jet printers and microscale bubble pump concepts.

© 2014 Elsevier Ltd. All rights reserved.

## 1. Introduction

The nucleation of bubbles on microscale surfaces immersed in subcooled liquids is important to several processes that transport fluids at the microscale, such as bubble pumps [1–5], mixers [2], and actuators [6,7]. Thermal inkjet printing [8–11] is the most prominent application of this concept. The nucleated bubbles exert a piston-like effect that pushes liquid through nozzles to form droplets that are directed to the paper through coordinated motion of the nozzles [12]. Inkjet technologies have also been applied to drug preparation [13] where the solvent consists of a mixture of ethanol, water, and glycerol. Other applications include deposition of polymers [14] proteins and cells [15,16], and 3D printing

technologies. A biosensor fabricated by inkjet printing of polymer and enzyme layers has also been reported [17].

In portable bubble pump processes, energy management is an important consideration. Conventional solid-state microheater configurations such as those employed in ink jet applications are fabricated onto a solid substrate (which we term “non back-side etched” NBSE microheaters) such as silicon. The substrate can be an effective thermal path during a power pulse [18] which makes the heating and phase change process inefficient. Solid-state microheater configurations that reduce heat losses will make the phase change process more energy efficient.

In this paper, we present a stress-minimized, suspended microheater for heating liquids. The design consists of a platinum (Pt) film deposited on a SiN membrane etched from the opposite side of the Pt heater, (i.e., a “back-side etched” (BSE) configuration). Results are reported that illustrate the capabilities of the BSE

\* Corresponding author.

E-mail address: [cta2@cornell.edu](mailto:cta2@cornell.edu) (C. Thomas Avedisian).

## Nomenclature

$C_2$ and $C_3$	capacitance filters (Fig. 9 and Table 1)	$R_p$	potentiometer resistance (Fig. 9)
$c_p$	specific heat	$R_{po}$	potentiometer resistance (Fig. 9) at balance point
DIP	dual-in-line package (Fig. 8)	$R_{so}$	internal resistance of DIP socket
$k$	thermal conductivity	$R_{wp}$	lead resistance of wires to bridge circuit
$L_{1,2}$	microheater dimensions (Fig. 2)	$R_{DIP}$	internal DIP resistance
$R_h$	microheater resistance	$t$	time
$R_{ho}$	room temperature microheater resistance	$t^*$	time during a power pulse at the inflection point (Figs. 1, 13, 14)
$R_{jumper}$	jumper resistors (Fig. 9)	$T$	temperature
$R_{PT3,PT4}$	resistances of platinum metallizations (Fig. 12)	$T_c$	critical temperature
$R_{LP}$	measured lead resistance for the pulse heating arrangement	$T_h$	average microheater temperature
$R_{LC}$	measured lead resistance for the heater calibration arrangement	$T_{ho}$	average microheater temperature at room temperature
$R_{mc}$	total measured resistance for calibration process	$T_{nuc}$	temperature at the started positions in Figs. 13 and 14
$R_{mp}$	total measured resistance for pulse heating (Figs. 9 and 12)	$\theta$	temperature coefficient of resistance (TCR)
$R_{mpo}$	total measured resistance for pulse heating at room temperature	$\rho$	density
		$V_{in}$	input voltage to the bridge circuit (Fig. 9)
		$V_{out}$	measured bridge output voltage (Fig. 9)

designs to nucleate bubbles with considerably less energy compared to more conventional substrate-supported NBSE microheaters. In addition, the microheater configurations provide an effective platform for accurately measuring the bubble nucleation temperature during a power pulse of microsecond duration.

Water was selected as the working fluid because of published data with which to compare measured nucleation temperatures [10,19–25], though the metrology developed is applicable to other fluids. The microheaters are immersed in subcooled water and heated with nominally square voltage pulses for durations ranging from 0.5  $\mu$ s to 10  $\mu$ s. This range is relevant to several industrial processes. The surface heating rate will be controlled by varying the pulse time and pulse amplitude.

## 2. Detecting bubble nucleation

When a bubble nucleates on a surface, liquid is displaced as the bubble grows. The microheater surface temperature increases and eventually the (relatively high thermal conductivity) liquid is displaced by the (comparatively low thermal conductivity) vapor and from there on the surface temperature increases in a manner consistent with it being in contact with a gas.

Fig. 1 schematically illustrates how the surface temperature may evolve under the conditions envisioned. The macroscopic manifestation of what is ostensibly a nano-scale process produces a temperature range ( $\Delta T$ ) over which the transition from solid/liquid to solid/gas contact occurs. Without direct visual evidence of the nucleation process [26–28] a mathematical definition of the spatially averaged nucleation temperature ( $T_{nuc}$ ) is taken to correspond to the inflection point,  $\frac{\partial^2 T}{\partial t^2} \Big|_{t=t^*} = 0$  [10].

## 3. Fabrication of BSE structures

The aspect ratio ( $L_1/L_2$ , see Fig. 2) of the BSE and NBSE microheaters used in the present experiments was 15:1 (i.e., 150  $\mu$ m long, 10  $\mu$ m wide, 200 nm thick). This ratio was considered to provide a reasonably uniform average temperature over the surface of the microheater. Heat transport to the connecting metallizations could be significant for very small aspect ratios (1:1) which would produce both a nonuniform and lower average temperature. This makes it more difficult to use the microheaters as a tool to measure the nucleation temperature. The microheater material employed

was Pt in view of its hardness and strong linear variation of electrical resistance with temperature.

The platinum metallization is structurally supported with either a thin SiN membrane or for comparison a SiO<sub>2</sub> backing layer on bulk Si. For traditional NBSE structures, backside heat losses are reduced by bonding to a low thermal conductivity material such as SiO<sub>2</sub>. The thermal resistance scales as  $\delta/k$  where  $\delta$  is thickness and the thermal conductivity  $k$  is comparatively small for SiO<sub>2</sub> [29]. As such, NBSE structures incorporated a SiO<sub>2</sub> backing with  $\delta_{SiO_2} = 2 \mu$ m. BSE structures need a backing for structural support during bubble nucleation, but it is desirable for this backing to be as thin as possible. This support was provided by a SiN layer with  $\delta_{SiN} = 0.2 \mu$ m.

Figs. 2a and 2b show side-view schematics of the BSE and NBSE configurations, while Fig. 2c shows a top view optical micrograph of a BSE device. The “microheater” itself is the metallization of length  $L_1$  and width  $L_2$ . The membrane consists of a rectangle upon which a 200 nm Pt/10 nm Ti layer is deposited and under which the Si substrate has been removed. In earlier tests, the 200 nm thick membranes were stable up to a size of 5 mm  $\times$  5 mm. The configurations employed in the present study incorporated a 200  $\mu$ m wide membrane. The fabrication sequence of BSE structures is illustrated in Fig. 3 [30]. Starting with a double-side pol-

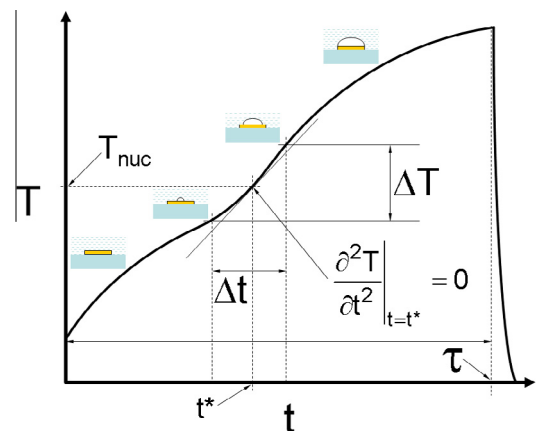
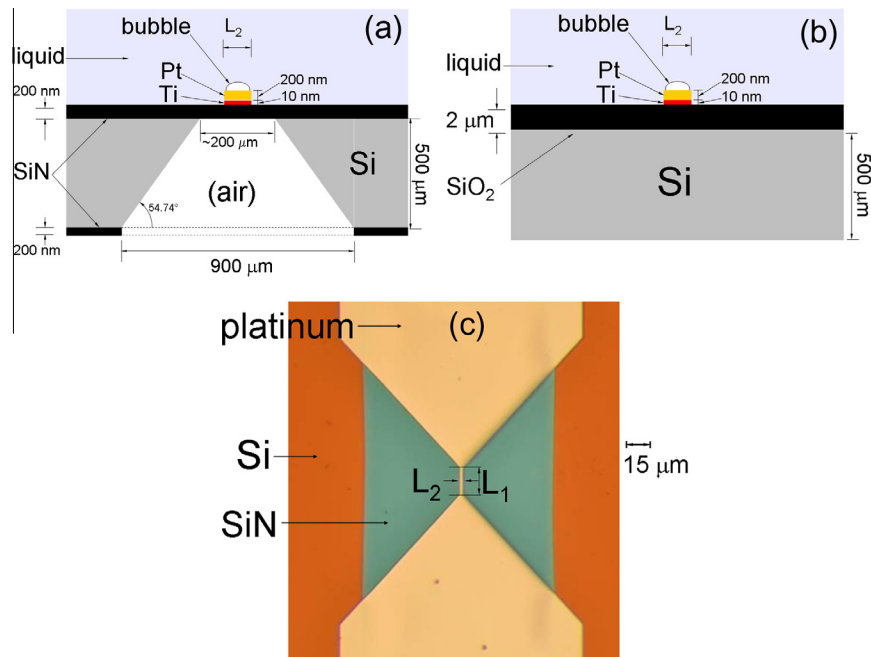
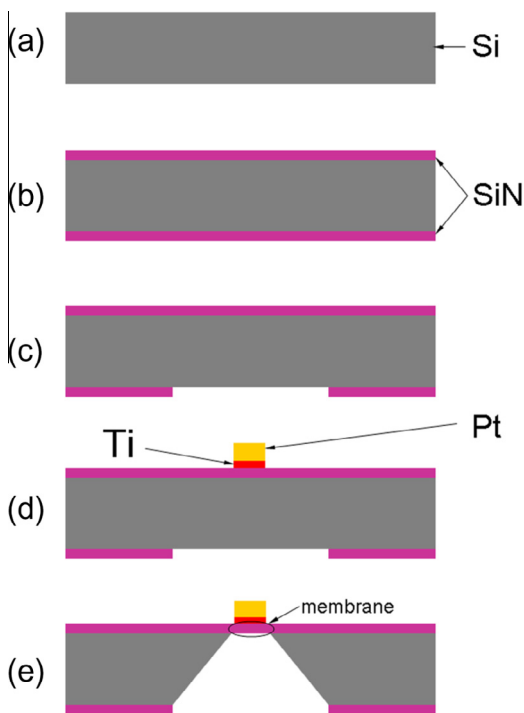


Fig. 1. Schematic of average microheater surface temperature during a power pulse. A bubble nucleation event centered at  $t^*$ , defined by the second derivative being zero, occurs over  $\Delta t$  and  $\Delta T$  for a voltage pulse of duration  $\tau$ .



**Fig. 2.** (a) Cross-sectional schematic of a BSE configuration (not to scale). (b) Cross-sectional schematic of a NBSE configuration (not to scale). (c) Photomicrograph of the thin film structure; the microheater is the region  $L_1 \times L_2$ .



**Fig. 3.** Schematic of steps to fabricate the BSE structures (not to scale): (a) polished 100  $\mu\text{m}$  thick Si wafer; (b) 200 nm low-stress SiN film is grown on both sides of the wafer; (c) SiN is etched on the back side; (d) a 200 nm platinum feature is patterned on the front side of the wafer using a backside mask aligner to orient the metal relative to the membrane; (e) the wafer is etched on the backside using KOH to create the membrane and form the microheater.

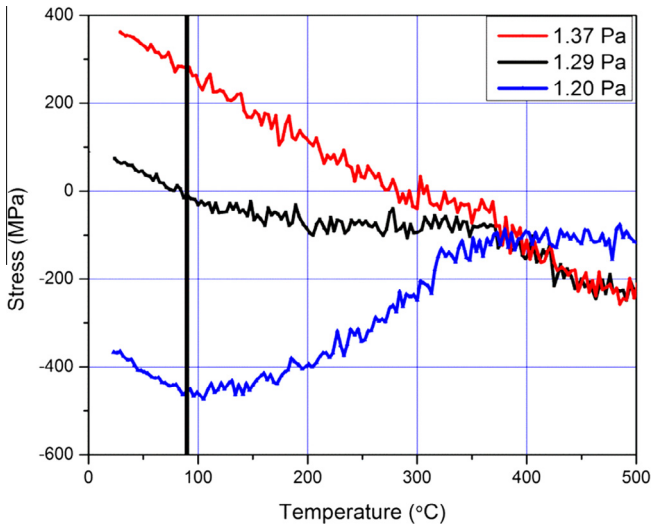
ished wafer (Fig. 3a), Low Pressure Chemical Vapor Deposition (LPCVD) was used to deposit 200 nm of low stress SiN on both sides of the Si wafer (Fig. 3b). The stress on the SiN film was approximately 200 MPa tensile. This small tensile stress is needed to keep the membrane from wrinkling once it is released in the

etching process. The front SiN was used for the membrane and the backside SiN was the etch mask material. The backside SiN was patterned and etched to make an opening in the Si for etching the Si (Fig. 3c). Next, a 200 nm Pt film over a 10 nm Ti adhesion layer was deposited and patterned (Fig. 3d). This was done before devices were etched, as the membranes are too fragile for the photolithography steps. The etching was performed by placing the wafer in a 90  $^\circ\text{C}$  bath of KOH (Fig. 3e). The etch time was in the range of (5–6) hours depending on the thickness of the wafer. The etch proceeded until the Si was completely removed in the exposed area, which then released the membrane. The wafer was then passivated with HCl, and rinsed in isopropanol and dried.

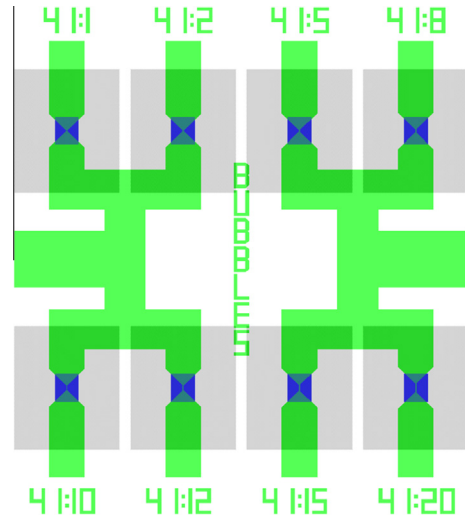
A key aspect of the metal deposition was to minimize the stress, and ensure the best compatibility with the thin SiN. A highly stressed Pt heater could rip the membrane apart at the end of the etch when the membrane is suddenly released from the silicon. Sputter deposition was selected to produce the Pt films, because the initial film stress (before annealing) is directly related to the deposition pressure, a parameter that was easy to control.

Fig. 4 shows the variation of stress (as measured with a Toho Technologies FLX-2320 thin film stress measurement system [31]) with temperature for three deposition pressures. At 1.29 Pa, the stress was found to be nearly zero at the etch temperature of 90  $^\circ\text{C}$ , so this pressure was used for all Pt depositions. A bi-layer lift-off process was used to configure the Pt metallization into the shape shown in Fig. 2c. Fig. 5 is a three-dimensional atomic force microscope (AFM) image of part of a single 2  $\mu\text{m}$  wide microheater (cf., the narrow section shown in Fig. 2c) that illustrates the feature resolution of the fabricated films. AFM cross sectional measurements are shown in Fig. 6 for the different heater widths fabricated ( $L_1$  in Fig. 2c).

Fig. 7 is a diagram of a microheater arrangement on a single device. Eight heater widths were examined with aspect ratios from 1 to 20. Any one of them could be powered through appropriate wiring configurations, though all are flooded with liquid at the same time during an experiment. The devices were mounted on a standard 40-pin dual-inline-package (DIP) prior to wirebonding



**Fig. 4.** Variation of initial membrane stress with temperature at three deposition pressures. The vertical black line represents the temperature of the KOH etch bath where it is desirable to have minimum stress when the etch is completed and the membrane is released.



**Fig. 7.** Illustration from the L-edit design software showing eight heaters with aspect ratios from 1 to 20. The light gray area is the opening on the back of the Si wafer where the etch takes place. Blue zones indicate the SiN membranes over which the Pt microheaters are suspended. (For interpretation of the references to color in this figure legend, the reader is referred to the web version of this article.)

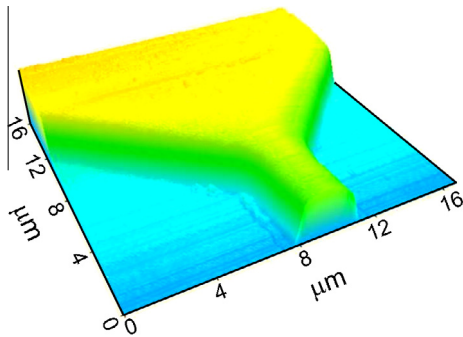


**Fig. 5.** Three-dimensional atomic force microscope (AFM) image of part of a single nominally 2 μm wide microheater that illustrates the feature resolution of the fabricated films.

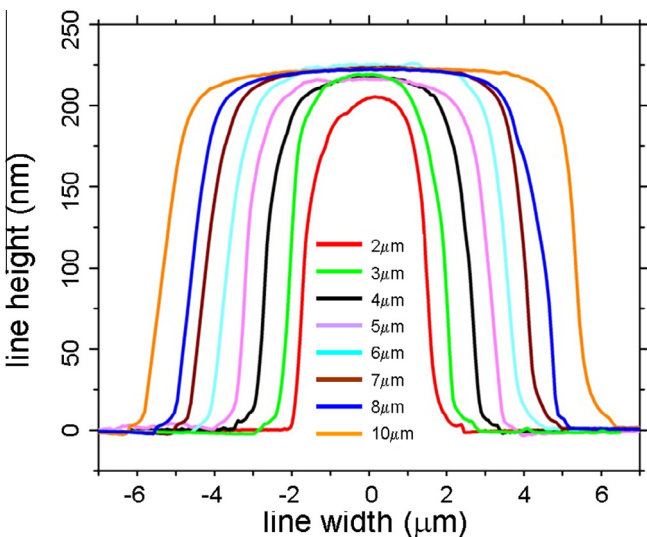


**Fig. 6.** AFM cross sectional measurements of eight different heater widths (scans across  $L_2$  in Fig. 2).

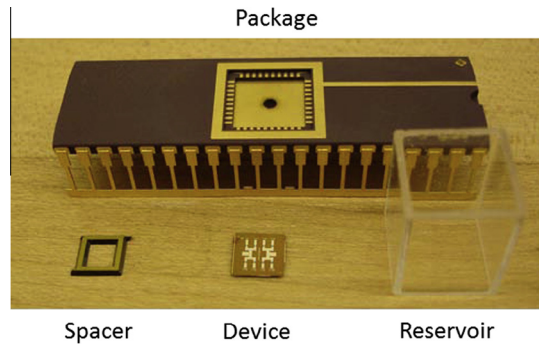


**Fig. 8.** Photograph of a new dual-in-line package prior to assembly with a microheater device. Vent hole for a BSE device is shown in the middle of the package.

and testing (Fig. 8). For NBSE structures the devices were attached to the center of the DIP with epoxy and allowed to set overnight before wire bonding. For BSE devices, the backside was vented to prevent the possible bursting of the membranes during the heating process due to pressurizing the air on the back side. This was accomplished by mounting the devices onto a spacer that was glued to the DIP which had a hole drilled into it (Fig. 8 shows the hole in the DIP).

The final packaging issue concerned the containment of the test liquid. It was desirable to prevent the heater from being operated without liquid present due to the risk of overheating and burnout of the heater. Due to the comparatively high surface tension of water, sessile drops will form on a device that remain for an hour or more (at room temperature) without spreading over the edges. As such, no special arrangement was needed to contain the liquid when water was tested. However, for fluids with lower surface tension (e.g., hydrocarbons and alcohols), the liquid will evaporate more quickly and tend to spread over a larger region. To confine such fluids, a cuvette with the bottom removed was attached to the DIP to provide four walls that created a reservoir of liquid over the chip.

## 4. Experiment

### 4.1. Bridge circuit

The microheaters were used as both a heater and temperature sensor. They were incorporated into one leg of the Wheatstone bridge circuit shown in Fig. 9. The bridge measures the response from a baseline (i.e., room temperature) for a constant  $V_{in}(t)$ . The circuit includes capacitive and inductive filtering to reduce electrical noise associated with high frequency short duration pulses imparted to the metal films by  $V_{in}(t)$ . The evolution of output voltage across the bridge  $V_{out}(t)$  was digitally recorded and subsequently converted to temperature with the aid of a separate calibration process as noted in Section 4.2. Table 1 lists the component values used.

The resistance of the leg opposing  $R_h$  is comprised of a fixed resistance,  $R_{jumper}$  ( $=R_3, 6$  or  $7$  in Fig. 9) that is selectable to adjust to changes in  $R_h$ , and a variable resistor,  $R_p$  (Bourns, Inc., (Riverside, Ca.) #3296W-1-200LF potentiometer or selectable “trimmer”) to finely tune the resistance of that leg during balancing. A programmed voltage  $V_{in}$  of duration  $\tau$  from a pulse generator (Agilent Model 8114A pulse generator) induces resistive heating primarily where the platinum necks down to the  $L_1 \times L_2$  region shown in Fig. 2c. A digital oscilloscope (LeCroy WaveRunner Model 44xi 5Gs/s digital oscilloscope) records the evolution of  $V_{out}$  associated with the change in  $R_h$  through a differential amplifier (LeCroy Model AP033), and the data are stored on a PC.

The electrical resistance of a microheater element is obtained from a two-point measurement as suggested by Fig. 9. A number of resistances in the connections leading up to the microheaters on the devices must be factored into measuring  $R_h$  when the DIP is connected to the oscilloscope or multimeter with various connecting wires and mounts. These additional resistances are associated with the lead wires, DIP, DIP socket, wirebonds, and platinum

**Table 1**

Component values in bridge circuit (Fig. 9).

Component	Value
$R_1$	46.2 $\Omega$
$R_3$	5.57 $\Omega$
$R_4 = R_5$	4.30 $\Omega$
$R_p$	0.2–19.5 $\Omega$ (adjustable)
$R_h$	Microheater resistance
$C_1$	500 $\mu$ F
$C_2$	250 pF
$C_3$	250 pF
$L$	$\sim$ 20 nH

metallization leading up to the microheater (Fig. 12). The sum of these resistances in series with the microheaters is given as

$$R_{LP} = R_{wires3} + R_{so3} + R_{DIP3} + R_{wb3} + R_{PT3,R} + R_{PT3,T} + R_{wires4} + R_{so4} + R_{DIP4} + R_{wb4} + R_{PT4,R} + R_{PT4,T} \quad (1)$$

where variables with the same subscript (either “3” or “4”) correspond to resistances on the same side of a heater.  $R_{LP}$  is treated as a constant during pulsing operations since the resistor components in eq. (1) are assumed to remain at room temperature during a power pulse.

The total resistance recorded by the oscilloscope or multimeter is  $R_{mp}$  and  $R_h$  is related to it as

$$R_h = R_{mp} - R_{LP} \quad (2)$$

At room temperature (subscript “o”)

$$R_{mpo} = R_{ho} + R_{LP} \quad (3)$$

$R_{mp}$  is related to  $V_{out}$  through standard (balanced) bridge relations as

$$R_{mp} = R_{po} \frac{1 - \frac{V_{out}}{V_{in}} \frac{R_{po} + R_{jumper} + R_1}{R_{po} + R_{jumper}}}{1 + \frac{V_{out}}{V_{in}} \frac{R_{po} + R_{jumper} + R_1}{R_1}} \quad (4)$$

(the evolution of  $V_{out}$  conforms to the schematic of Fig. 1). With  $R_h$  known from Eqs. (1)–(4), the average microheater temperature is obtained from a calibration that assumes a linear relationship with temperature in the form

$$T = \frac{1}{\theta} \left( \frac{R_h}{R_{ho}} - 1 \right) + T_o \quad (5)$$

where  $\theta$  is the “temperature coefficient of resistance” (TCR). The calibration relating  $R_h$  to  $T$  is discussed in Section 4.2.

Before an experiment the bridge is “balanced” such that  $R_h + R_{LP} \approx R_p + R_{jumper}$  (Fig. 9). Of these resistors  $R_p$  is tuneable. A value of approximately  $V_{in} = 0.8$  V was employed in balancing as this was the smallest voltage commensurate with the overall impedance of the circuit without  $R_h$  being heated. During balancing,  $\tau$  was fixed at 5  $\mu$ s and the bridge pulsed at 20 Hz. Once balanced at room temperature,  $R_p$  is not changed (i.e.,  $R_p = R_{po}$ ). For an applied pulse large enough to cause heating in the microheater, the bridge becomes “unbalanced” due to  $R_h$  changing.

The bridge is not an entirely pure resistance circuit. The rapid rise and fall of the applied voltage pulse, combined with the reactive components of the circuit will lead to voltage spikes in the  $V_{out}(t)$  signal which can impact the precision of measuring the inflection point temperature (Fig. 1). The circuit diagram includes intrinsic bridge inductances,  $L_{i1}$  and  $L_{i2}$ , which need to be compensated to reduce their affect on the output signal. An example of the voltage spikes that can be produced is shown in Fig. 10a. To counter this effect inductive and capacitance filtering was integrated into the bridge circuit as shown in Fig. 9. The  $C_1$  capacitor filters

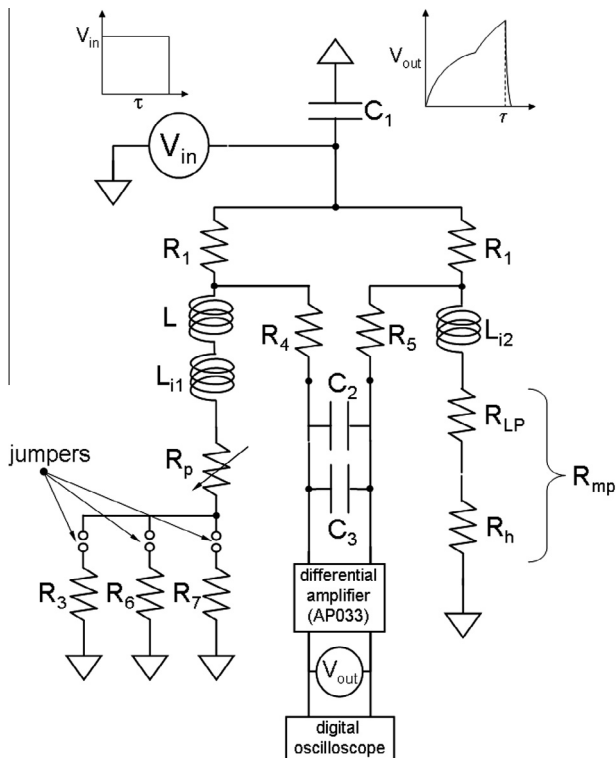


**Fig. 9.** Schematic of bridge circuit. Component values are given in Table 1.

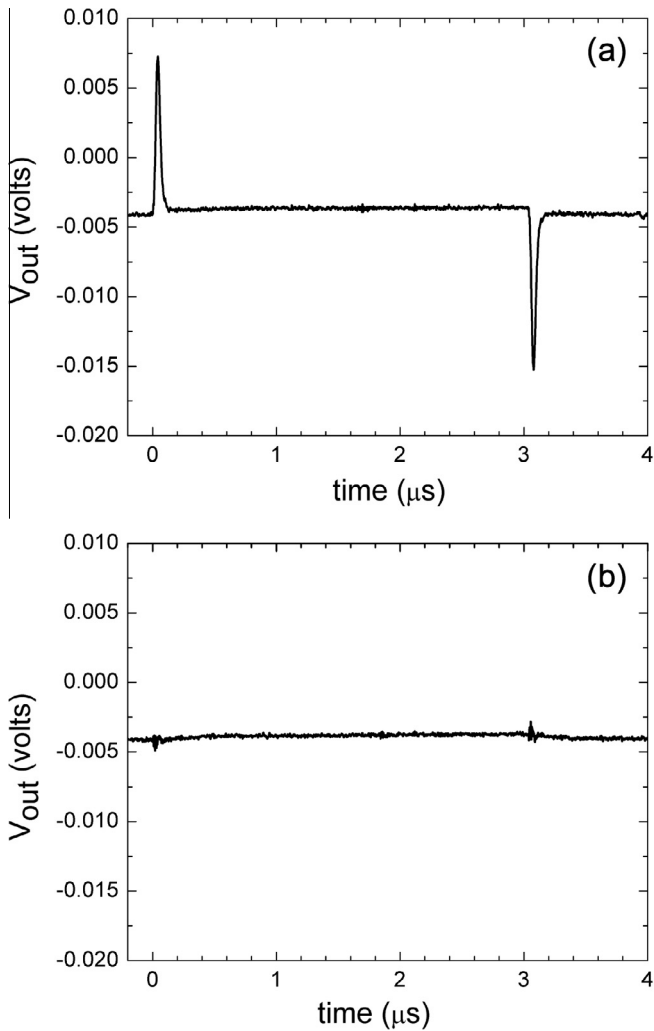


**Fig. 10.** Evolution of  $V_{out}$  for balancing a NBSE configuration in the bridge circuit (Fig. 9) for  $V_{in} \approx 0.8$  V: (a) bridge without an inductor; (b) bridge with an inductor. The voltage spikes at the beginning and end of the pulse are due to electrical noise that the filter and inductor are used to minimize.

the signal generator while the  $C_2$  and  $C_3$  capacitors are simple first-order filters.

A variable inductor,  $L$ , was included in the bridge to minimize the influence of the intrinsic inductances on output signal by balancing the inductive reactance of the bridge. The inductor was a simple hand-wound coil with an estimated inductance of approximately 20 nH. The coil was adjusted by hand in an *ad hoc* manner (i.e., spreading or compressing the coils) until the voltage spikes were minimized, which essentially corresponds to  $L = L_{12} - L_{11}$ . The efficacy of adjusting  $L$  to minimize spikes in  $V_{out}$  is shown by comparing Fig. 10a and b for a nominally 3  $\mu s$  pulse. By adjusting  $L$ , the spikes in Fig. 10a are all but removed as shown in Fig. 10b.

#### 4.2. Thermal conditioning and calibration of microheaters

The electrical resistance of the device will change due to thermal cycling in the calibration and pulsing operations. The effect may be due to material annealing during heating and cooling cycles, which has also been noted for thermal ink-jet print heads [10]. The electrical resistance must be stabilized before systematic pulsing experiments and nucleation temperature measurements can be carried out. Microheaters were thermally stressed in operations that involved passively cycling their temperature in an oven

until the electrical resistance was stabilized, then pulsing them with  $V_{in}(t)$  to simulate the thermal shock conditions of systematic experiments to measure  $V_{out}(t)$ .

Temperature cycling was carried out by placing DIPs with microheater devices in a computer-controlled furnace (Thermolyne 48000) that was interfaced with a Keithley 2001 multimeter. The oven was cycled under computer control between room temperature and approximately 260 °C (at higher temperatures the integrity of the adhesive that attaches the chip to the DIP would fail). The oven heating rate was approximately 1 °C/min, which was low enough to ensure thermal equilibrium during the cycling process.

The time to reach the maximum pre-set temperature was approximately 4 h. The cooling process could not be controlled, however, and the DIP was brought back to room temperature and allowing the temperature to drop by natural convection. The cool-down time was approximately 12 h. The time to execute one up/down cycle was therefore about 16 h. Depending on the

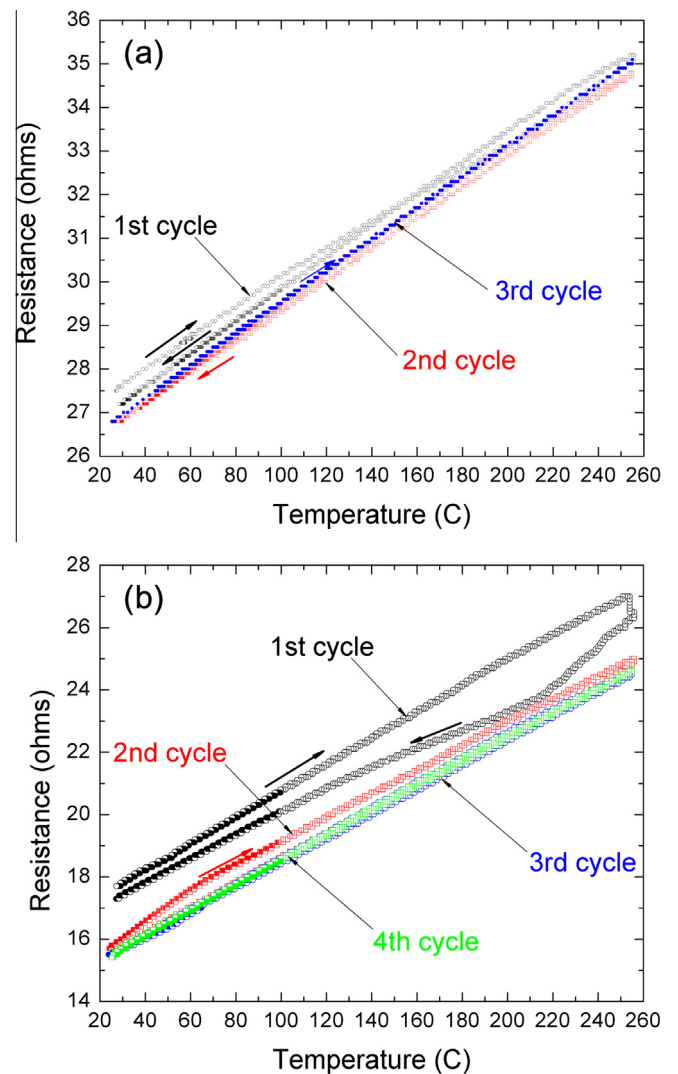


**Fig. 11.** (a) Calibration cycle of a 15:1 aspect ratio 2  $\mu m$  wide microheaters showing the effect of temperature cycling: after the third cycle the resistance did not change and the third cycle data were used to obtain the TCR (Eq. (5)). (b) Calibration cycle for a BSE microheater: after four cycles, the resistance did not change. Arrows in the figures indicate the direction of varying temperature for the first cycle. As part of thermal conditioning, the microheaters were subjected to systematic pulsing at 75 Hz after oven cycling with pulse widths between 10  $\mu s$  and 0.5  $\mu s$  and with  $V_{in}$  selected so that the inflection point was positioned at approximately 80% of the pulse time.

number of heating and cooling cycles, the time to condition the microheaters by oven cycling was typically about three days of continuous operation.

Fig. 11 shows the variation of measured resistance of the microheater and metallization ( $R_{PT}$ ) with temperature for three (Fig. 11a) and four (Fig. 11b) cycles. A progressive merging of the measurements is evident, with the resistance decreasing with each up/down cycle until eventually it did not change (e.g., after the third cycle for the NBSE microheater (Fig. 11a) and the fourth cycle for the BSE microheater (Fig. 11b)). The number of cycles to achieve a stabilized resistance was typically three to five.

Following the oven temperature cycling, the DIP was removed from the furnace, placed in the bridge circuit, and the device immersed in water. It was then subjected to pulsing at 75 Hz with pulse widths between 10  $\mu$ s and 0.5  $\mu$ s and with  $V_{in}$  selected so that the inflection point was positioned at approximately 80% of the pulse time. The intent of this pulsing operation was to examine performance under the thermal shock conditions of pulse heating. For all microheaters employed in this study, the variation of resistance with temperature following the last oven cycle did not change after these pulsing operations.

It is important to note that the measured resistance from the oven cycling operations,  $R_{mc}$ , is the sum of all resistances in the network between the device and multimeter. It is similar to  $R_{mp}$  (Eq. (2)) during pulsing experiments (Fig. 12), but also includes extra wires and an additional socket for the DIP, which are part of the cycling apparatus. The combined resistance of the lead wires, DIP, DIP socket, wirebonds, and additional wires and socket is  $R_{LC}$ , which is similar to  $R_{LP}$  from the pulsing operations. However, unlike  $R_{LP}$ ,  $R_{LC}$  includes additional resistances associated with lead wires and socket in the temperature cycling apparatus, but not the resistance of the platinum metallizations leading up to the microheater.

The resistance of the metallization and heater,  $R_{PT}$ , which is shown schematically in Fig. 12 is related to  $R_{mc}$  and  $R_{LC}$  as

$$R_{PT}(T) = R_{mc}(T) - R_{LC}(T) \quad (6)$$

where  $R_{LC}(T)$  is obtained by shunting two attachment pads on the DIP with wirebond material of essentially the same length as used in attaching the microheaters to the DIP. The shunted DIP/

socket/wirebond arrangement was then cycled in the oven over the same temperature range as the microheater.  $R_{LC}$  was found to be approximately 1.9  $\Omega$  at room temperature and 2.7  $\Omega$  at 250  $^{\circ}$ C.

A line was fit to the  $R_{PT}(T)/R_{PT0}$  curve (where  $R_{PT0}$  is the room temperature resistance of the platinum metal) for the final oven cycling, and the slope of the line is the TCR ( $\theta$ ), as determined from Eq. (3). Note that in this calculation,  $R_{PT}/R_{PT0}$  is a valid substitution for  $R_h/R_{h0}$  in Eq. (3) since all of the platinum metal heats up during the oven cycling operations; conversely, during pulsing experiments, this would not be a valid substitution since only the microheater is assumed to rise in temperature. Using this procedure, it was found that the TCRs for the two heater configurations were  $\theta_{BSE} = 0.00270 \text{ }^{\circ}\text{C}^{-1}$  and  $\theta_{NBSE} = 0.00134 \text{ }^{\circ}\text{C}^{-1}$ .

#### 4.3. Measurement of average nucleation temperature

The BSE and NBSE configurations were systematically pulsed in the bridge circuit to measure the evolution of  $V_{out}$  for the following pulse widths: 10  $\mu$ s, 5  $\mu$ s, 3  $\mu$ s, 2  $\mu$ s, 1.5  $\mu$ s, 1  $\mu$ s, and 750 ns (as well as 500 ns for the NBSE heater). For each value of  $\tau$ , an average of 500  $V_{in}(t)$  pulses at 20 Hz provided  $V_{out}(t)$  measurements that were stored as a running average in the oscilloscope, along with the pulse generator impedance for each pulse width examined.

To facilitate identification of nucleation,  $V_{in}$  was set for each pulse width so that the inflection point was positioned at approximately  $t^* = 0.8 \tau$  in Fig. 1b. Positioning the inflection point at earlier times during a pulsing operation risked the average temperature of the microheater exceeding the melting point of platinum during the vapor-phase heating portion (Fig. 1a). For later times, the amount of data available for processing to determine the nucleation temperature would be limited.

During pulsing  $R_h$  is obtained from Eqs. (2) and (3),

$$R_h = R_{ho} + (R_{mp} - R_{mpo}) \quad (7)$$

$R_{mpo}$  and  $R_{ho}$  are found only after  $R_h$  has stabilized following oven cycling operations.  $R_{mpo}$  is determined by simply connecting the DIP to a multimeter.  $R_{ho}$  was computed using the concept of a resistance per unit square,  $A_o$ , for thin films that are uniform in thickness:

$$R_{ho} = 15 A_o \quad (8)$$

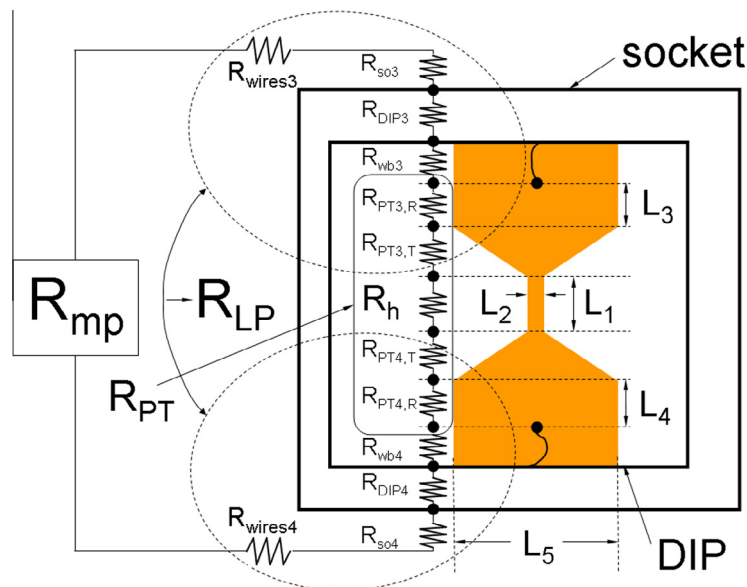


Fig. 12. Schematic of resistance network for determining the microheater resistance ( $R_h$ ) from the measured total resistance,  $R_{mp}$ .

Determining  $A_0$  requires an examination of the resistances that comprise the network displayed in Fig. 12. In Eq. (1) it is assumed that  $R_{wires3} = R_{wires4}$ ,  $R_{so3} = R_{so4}$ ,  $R_{DIP3} = R_{DIP4}$ ,  $R_{wb3} = R_{wb4}$ , and  $R_{PT3,T} = R_{PT4,T}$  (the trapezoidal sections of the platinum metallization). Due to the asymmetrical placement of the wirebonds on opposite sides of the heater,  $R_{PT3,R}$  and  $R_{PT4,R}$  (the rectangular sections of the platinum metallization) are assumed to be the only contributions to differences in  $R_{LP}$  for heaters of different aspect ratios.

$A_0$  is related to  $R_{mpo}$  and  $R_{mpo1:1}$  as

$$A_0 = \frac{R_{mpo} - R_{mpo1:1}}{\left[ \left( \left( \frac{L_3}{L_5} \right)_{15.1} + \left( \frac{L_4}{L_5} \right)_{15.1} \right) - \left( \left( \frac{L_3}{L_5} \right)_{1:1} + \left( \frac{L_4}{L_5} \right)_{1:1} \right) + 14 \right]} \quad (9)$$

where  $R_{PT3,R} = A_0 \left( \frac{L_3}{L_5} \right)$  and  $R_{PT4,R} = A_0 \left( \frac{L_4}{L_5} \right)$  was used and only the number of “squares” comprising a microheater and the rectangular section of the metallizations is responsible for the difference between  $R_{mpo}$  and  $R_{mpo1:1}$ .  $L_3$  and  $L_4$  were obtained from photomicrographs of the microheaters (cf., Fig. 2c), and  $R_{mpo1:1}$  is the measured resistance at room temperature of a microheater with an aspect ratio of 1:1 (i.e., Fig. 7, upper left corner, shows such a configuration). Note that none of the individual resistances that make up  $R_{LP}$  (Eq. (1)) need to be computed to determine  $A_0$ . Using Eqs. (8) and (9) for the hardware used in this study, it was found that  $R_{ho} = 10.48 \Omega$  for a BSE configuration and  $R_{ho} = 18.00 \Omega$  for a NBSE configuration. Using Eq. (4) to convert measured  $V_{out}$  values to  $R_{mp}$ , and Eq. (7) to relate  $R_{mp}$  to  $R_h$ , Eq. (5) was used to convert  $R_h$  to the average microheater temperature.

With the average nucleation temperatures known, the inflection point temperatures were obtained by fitting the evolution of average microheater temperature with a piecewise cubic polynomial spline fitting program [32]. The polynomial was then differentiated in each segment to obtain the heating rate and second derivative. A function in the MATLAB library facilitated determining first and second derivatives at  $t^*$ .

Uncertainties in the nucleation temperature arise in part from instrumentation precision, the calibration process (e.g., the accuracy of the TCR), the assumptions discussed earlier in Section 4.3 and the ability to fit the evolution of temperature to a cubic spline polynomial and differentiating the result to obtain  $T_{nuc}$ . While the fitting and differentiation processes were able to determine the nucleation temperature for the larger pulse widths with high confidence, larger uncertainties existed for shorter pulse widths where the inflection points were less distinct. The estimated uncertainty in reported nucleation temperatures (Tables 2 and 3) is up to approximately  $\pm 3\%$ .

## 5. Results and discussion

Figs. 13 and 14 show the evolution of average microheater temperature with time for the indicated  $\tau$  and  $V_{in}$  for NBSE and BSE microheaters, respectively. The asterisks on the temperature traces indicate the nucleation temperatures for the conditions indicated

**Table 2**

Nucleation temperatures and corresponding heating rates for NBSE configurations (Fig. 13). The indicated time ( $t^*$ ) is after the initiation of the power pulse.

$T_{nuc}$ (°C)	Heating rate (°C/s)	$t^*$ ( $\mu$ s)	Pulse width ( $\mu$ s)
282.2	$4.84 \times 10^6$	7.88	10
286.7	$2.24 \times 10^7$	3.72	5
291.3	$6.72 \times 10^7$	2.21	3
296.1	$1.06 \times 10^8$	1.50	2
298.7	$2.85 \times 10^8$	1.19	1.5
301.9	$3.29 \times 10^8$	0.749	1
303.6	$5.98 \times 10^8$	0.584	0.75
304.8	$6.63 \times 10^8$	0.382	0.50

**Table 3**

Nucleation temperatures and corresponding heating rates for BSE configurations (Fig. 14). The indicated time ( $t^*$ ) is after the initiation of the power pulse.

$T_{nuc}$ (°C)	Heating rate (°C/s)	$t^*$ ( $\mu$ s)	Pulse width ( $\mu$ s)
271.5	$7.82 \times 10^6$	8.27	10
266.1	$2.59 \times 10^7$	3.80	5
274.4	$6.50 \times 10^7$	2.42	3
277.2	$1.17 \times 10^8$	1.49	2
277.6	$2.05 \times 10^8$	1.12	1.5
280.3	$2.72 \times 10^8$	0.794	1
293.5	$4.73 \times 10^8$	0.637	0.75

on the figures. The nucleation temperatures are quite high as shown in Figs. 13 and 14 with superheats of well over one hundred degrees (e.g., compared to water's normal boiling point of 100 °C and superheats of a few degrees traditionally found in nucleate boiling processes).

The evolution of average microheater temperatures in Figs. 13 and 14 is consistent with the trends shown in schematic form in Fig. 1 for both the NBSE (Fig. 13) and BSE (Fig. 14). Two tracks are shown from the data in Figs. 13 and 14 at each pulse time: one associated with liquid-only heating and the other arising from heat transfer between the microheater surface and vapor from nucleated bubbles that spread over the surface. At  $\tau = 10 \mu$ s a small reduction in temperature was observed at nucleation. This effect indicates localized cooling when nucleation occurs, which could arise by a growth/collapse cycle as in traditional boiling where cold liquid is drawn to the surface as the bubble grows (comparatively slowly) into the subcooled liquid that leads to a momentary quenching of the surface [19].

As the pulse time decreases, the temperature drop shown at  $\tau = 10 \mu$ s in Figs. 13 and 14 disappears. The surface temperature is increasing apparently at a faster rate than for bubbles to grow and collapse to produce heating and quenching cycles [19]. For the BSE configuration the change in heating rate across the inflection point temperature is slightly sharper than the NBSE configuration (cf.,  $\tau = 1.5 \mu$ s in Figs. 13 and 14). With increasing nucleation temperature, the microheaters will be at higher average temperatures. As the critical point is approached the convergence of properties (e.g., thermal conductivity) will make the transition across the inflection point more gradual, which is reflected in Figs. 13 and 14 by comparing the evolution of temperature for  $\tau = 5 \mu$ s with  $\tau = 0.75 \mu$ s.

Fig. 15 shows the variation of nucleation temperatures with heating rates as obtained from the data in Figs. 13 and 14. Tables 2 and 3 list the data. The nucleation temperatures for the two heater configurations differ by between 10 C and 20 C. At the highest heating rates the difference is about 11 C. The trend lines shown in Fig. 15 are suggestive of a convergence of the nucleation temperature. In terms of reduced temperature ( $T/T_c$  (K/K)) at the shortest pulse times and highest heating rates  $T/T_c = 0.89$  for the NBSE heater while for the BSE configuration  $T/T_c = 0.87$ . These reduced temperatures are close to 90% of the critical temperature which is typical of liquids at their theoretical superheat limits under standard atmospheric pressure conditions.

For lower pulse times and heating rates, the nucleation temperatures are substantially below the homogeneous nucleation temperature of water, though still well above the normal boiling point of water. The traditional bubble nucleation process is one of bubbles forming at surface imperfections that trap gas and then grow to cover the heated surface. Prior work has shown superheats typical of this process to be a few tens of degrees [33], even for liquids in contact with surfaces characterized by nano-scale roughness [34] and heating rates that are orders of magnitude below the present study.

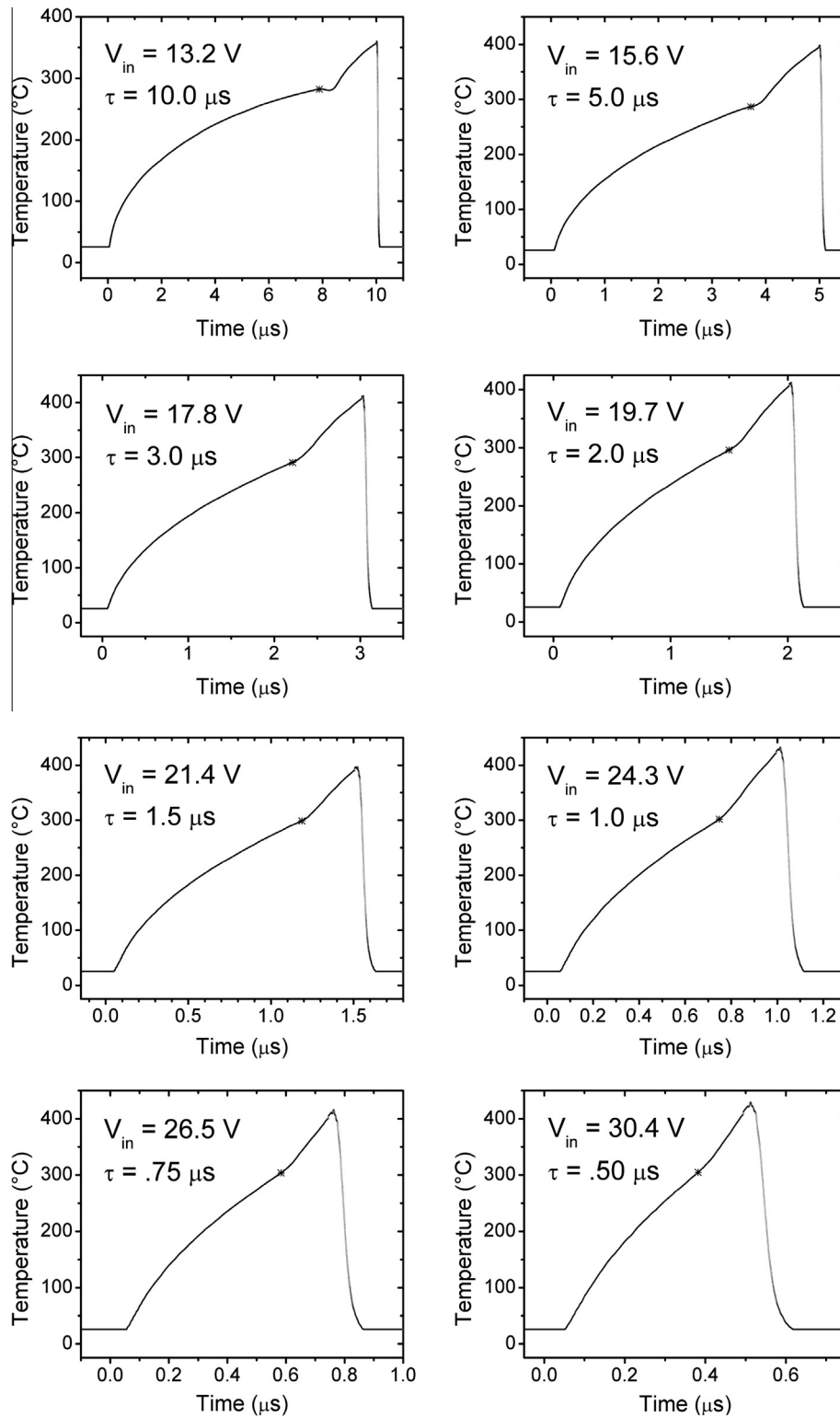


**Fig. 13.** Evolution of average platinum temperature for the indicated pulse width ( $\tau$ ) and  $V_{in}$  for a NBSE microheater. Traces shown are averaged over 500 individual pulses. Stars indicate the inflection points.

For especially fast transient heating processes bubbles could remain at the microheater surface at those locations where they are nucleated by traditional processes, while other parts of the same surface are devoid of bubbles. As the heating rate is increased the surface temperature increases while bubbles do not necessarily depart as in traditional surface boiling processes because the bub-

ble growth rate is not fast enough compared to rate of temperature increase [19]. A limit is eventually reached where bubbles form by a different mechanism than more traditional (low superheat) processes: random density fluctuations that form voids which attain a state of metastable equilibrium. The speculation is that this process could arise occur even though bubbles may already have

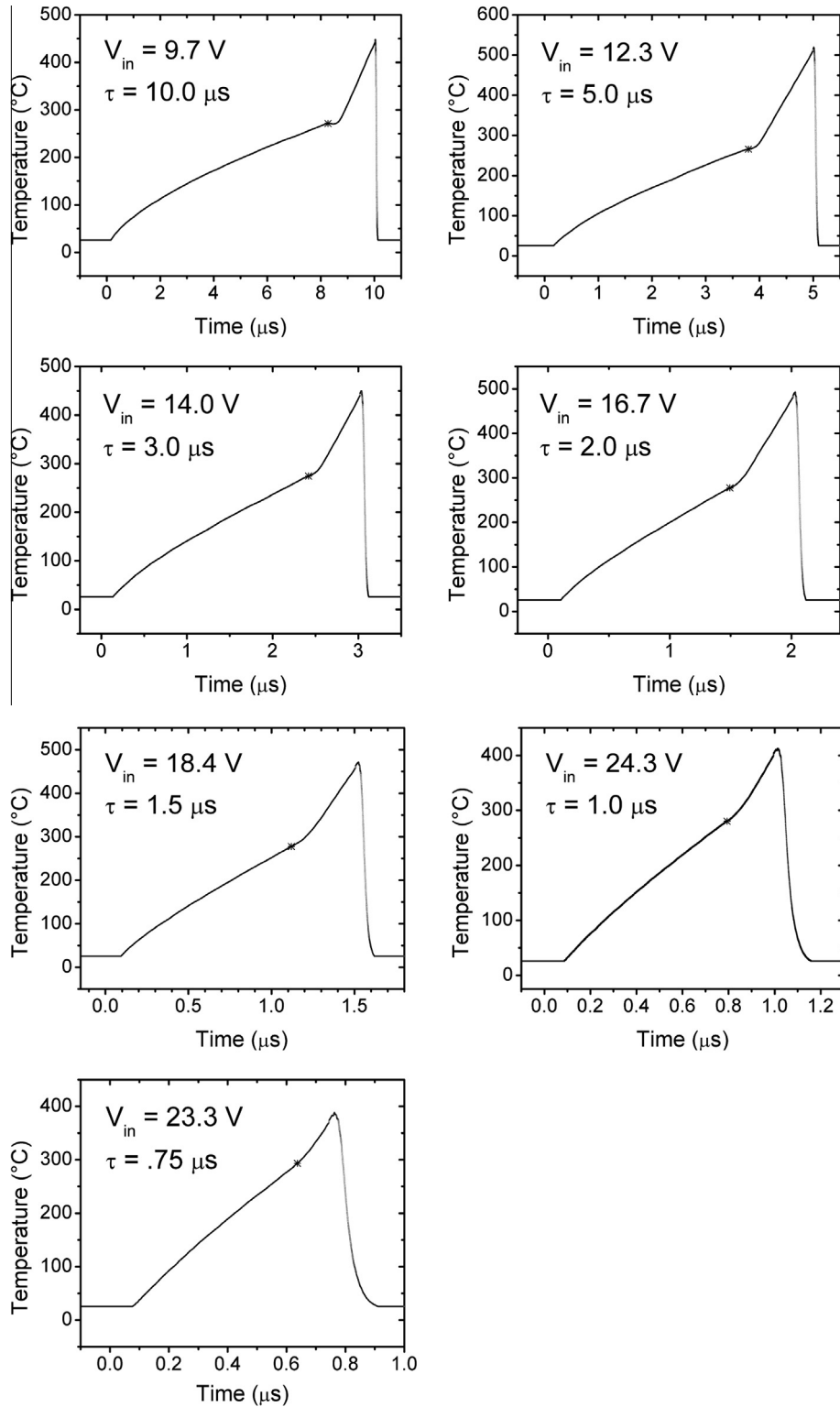


**Fig. 14.** Evolution of average platinum temperature for the indicated pulse width ( $\tau$ ) and  $V_{in}$  for a BSE microheater. Traces shown are averaged over 500 individual pulses. Stars indicate the inflection points.

formed by more traditional vapor trapping mechanisms at other locations on the surface. At very high heating rates the entire surface is covered by these vapor voids and a limit is reached above which no further superheat can be sustained. The liquid then transitions to vapor.

An alternative mechanism by which high liquid superheats can be sustained at a solid surface during rapid heating and cooling

cycles involves the role of fluid-wall attractive forces [35]. Very close to a heated surface (within a few nanometers) these forces can apparently increase the local pressure while the bulk fluid remains at a lower pressure. Bubble nucleation at the surface would then be suppressed by the locally higher pressures there. It then becomes possible for a bubble to nucleate first in the liquid near to, but not at, the solid with which it is in contact.

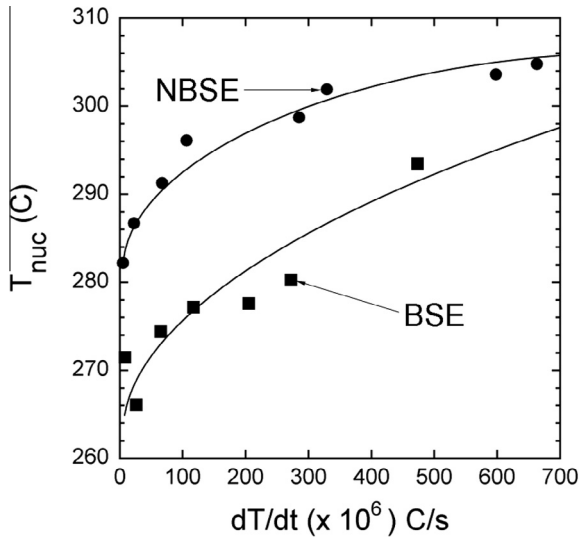


Fig. 15. Variation of measured inflection point (nucleation) temperatures with heating rates for NBSE (●) and BSE (■) configurations. Data come from Figs. 13 and 14 at  $t^*$ . Trend lines are shown.

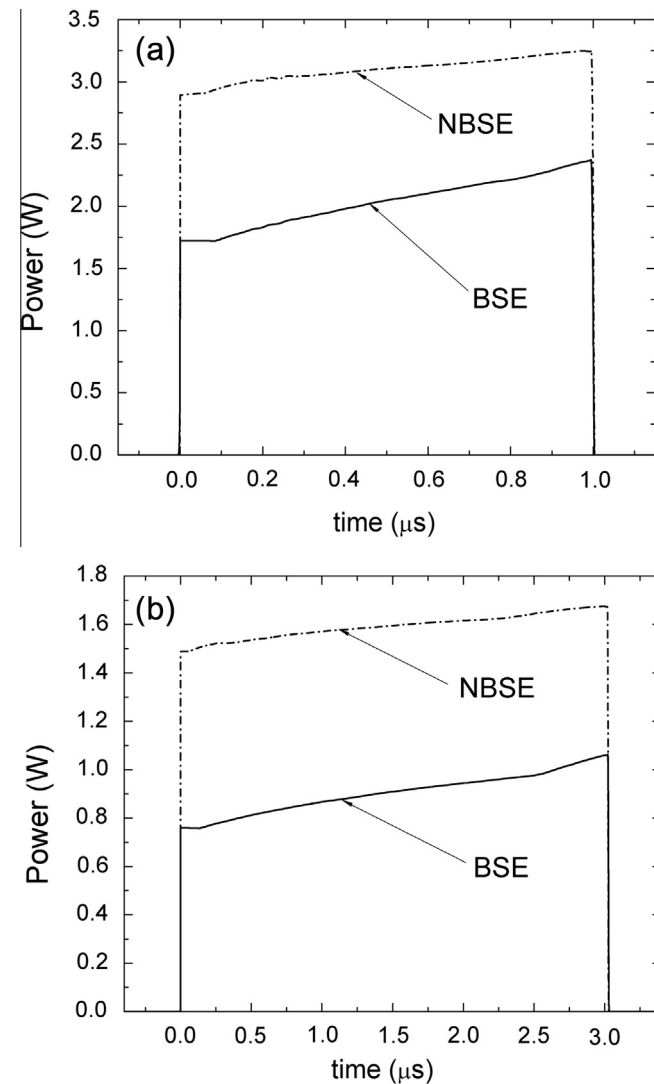


Fig. 16. Evolution of power for BSE and NBSE configurations at  $\tau = 1 \mu\text{s}$  (a) and  $\tau = 3 \mu\text{s}$  (b).

The evolution of power to the microheaters corresponding to the heating profiles of Figs. 13 and 14 is shown in Fig. 16 for two pulse times. For  $\tau = 1 \mu\text{s}$  (Fig. 16a) approximately 30% less power is needed to nucleate bubbles (which occurs at about  $0.77 \mu\text{s}$ ) for the BSE microheater compared to the NBSE microheater; for  $\tau = 3 \mu\text{s}$  (Fig. 16b) approximately 40% less power is needed to promote bubble nucleation on a BSE configuration compared to a NBSE configuration (which occurs at about  $2.3 \mu\text{s}$  for the NBSE). The fact that the power is not constant during the pulse is due to the dependence of  $R_h$  on temperature. Fig. 17 shows the ratio of BSE to NBSE power needed to nucleate bubbles as a function of pulse time. The reduced backside heat loss for BSE configurations is due to the insulating effect of air compared to NBSE configurations.

A simple model of heat transfer to the liquid and backside that considers the BSE and NBSE membrane configurations of Fig. 2 as semi-infinite solids shows how solid and fluid properties influence the heat fluxes to the liquid ( $q''_L$ ) and backside ( $q''_B$ ) for an imposed heat flux at the interface  $q''_i$  due to pulse-heating. These fluxes are related as [35]  $\frac{q''_L}{q''_B} = \frac{\gamma_L}{\gamma_B}$ , where the thermal effusivities  $\gamma_L$  and  $\gamma_B$  for the liquid and backside materials are defined as  $\gamma_{L,B} = \sqrt{k_{L,B}\rho_{L,B}c_{L,B}}$ . Materials with large effusivities will transport heat more effectively than those with smaller effusivities. Comparing BSE microheaters with air on the back side (i.e.,  $B = \text{air}$ ) to NBSE configurations with a solid (i.e., SiN or SiO<sub>2</sub>) on the back side ( $B = s$ ) shows that  $\gamma_L/\gamma_{\text{air}} \gg \gamma_L/\gamma_s$ . Though this model is not quantitative for the heater geometries of Fig. 2, the results are broadly consistent in that BSE heaters should be more effective at heating liquids compared to NBSE configurations.

It is noted that the slight differences in nucleation temperatures of the BSE and NBSE configurations for a given pulse time (Tables 2 and 3) would ostensibly be expected to lead to differences in energy needed to nucleate bubbles on the two configurations. However, we found that the energies needed to nucleate bubbles at the different temperatures were small for a given pulse time compared to the energy differences related to substrate heat losses noted above.

In addition to lowering substantially the power requirements to nucleate bubbles, the results showed the durability of the BSE configuration to function over thousands of pulse cycles. The only failure mode observed was inadvertent: exceeding operational temperatures that melted the metallization owing to not carefully

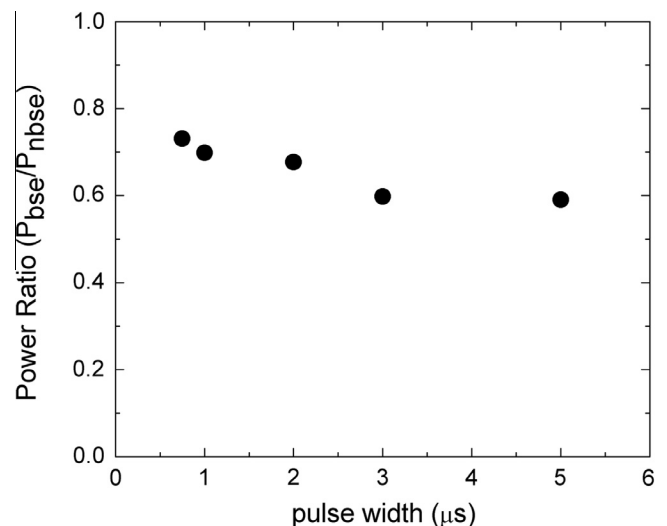


Fig. 17. Variation of ratio of BSE to NBSE power corresponding to the inflection point in Figs. 13 and 14 with pulse width.

controlling  $V_{in}$ . The greater power efficiency of BSE micro-heaters may be useful in devices that traditionally employ bubbles formed by nucleation to move fluids on the microscale, such as thermal inkjet printers and certain types of bubble pumps and actuators.

## 6. Summary

A process for fabricating platinum membrane thin film materials has been described that produces a stress-minimized, suspended metal film that was used for heating liquids. The configurations were used to determine the power requirements to initiate bubble nucleation in water under pulse-heating conditions. A new bridge circuit design was developed with capacitive and inductive filtering to measure the average membrane temperature with a minimal influence of electrical spikes originating from high frequency switching. The results were compared to conventional metal film structures fabricated on solid substrate materials.

The results show that bubble nucleation on the metal membrane structures requires considerably less power than conventional configurations fabricated on bulk solid materials. At the same time, there was no substantive difference in the superheat limit temperature for the two microheater configurations examined, confirming that the superheat limit is controlled by processes intrinsic to the liquids and not the microstructural configurations of the heaters. The onset of nucleation on membrane-supported metal films produces a slightly sharper inflection point compared to solid substrate-supported configurations. The reduced temperatures at the highest rates and shortest pulse times were found to approach the homogeneous nucleation temperature of water. The data reported suggest the potential of backside etching in applications to reduce the power needed to nucleate bubbles where power management is critical for long-term operation, such as in portable printing and bubble pump devices that rely on bubble nucleation at the superheat limit to transport fluids on the microscale.

## Conflict of interest

None declared.

## Acknowledgments

This project was supported in part by the National Institute of Standards and Technology (NIST, Gaithersburg, MD) and the Cornell University Engineering Learning Initiatives Program to EJC. Fabrication of the microheater structures was carried out at the NIST Center for Nanoscale Science and Technology (CNST). The contributions of Messrs. Robert Chen (Sensata Corp.), Jeremy Horwitz, and Jeff Rah (Cornell) are much appreciated. We also gratefully acknowledge the expertise of Mr. Christopher Montgomery (NIST) for assembly of the microheater devices into operational packages.

## References

- [1] H. Yuan, A. Prosperetti, The pumping effect of growing and collapsing bubbles in a tube, *J. Micromech. Microeng.* 9 (4) (1999) 402–413.
- [2] J.H. Tsai, L. Lin, Active microfluidic mixer and gas bubble filter driven by thermal bubble micropump, *Sens. Actuators A-Phys.* 97–98 (2002) 665–671.
- [3] Z.Z. Yin, A. Prosperetti, Blinking bubble micropump with microfabricated heaters, *J. Micromech. Microeng.* 15 (9) (2005) 1683–1691.
- [4] J.Y. Jung, H.Y. Kwak, Fabrication and testing of bubble powered micropumps using embedded microheater, *Microfluid Nanofluid* 3 (2) (2007) 161–169.
- [5] J. Suh, D. Cytrynowicz, F.M. Gerner, H.T. Henderson, A MEMS bubble pump for an electronic cooling device, *J. Micromech. Microeng.* 20 (12) (2010).
- [6] L. Lin, A.P. Pisano, Thermal bubble powered microactuators, *Microsyst. Technol.* 1 (1) (1994) 51–58.
- [7] M. Shikida, T. Imamura, S. Ukai, T. Miyaji, K. Sato, Fabrication of a bubble-driven arrayed actuator for a tactile display, *J. Micromech. Microeng.* 18 (6) (2008).
- [8] R.R. Allen, J.D. Meyer, W.R. Knight, Thermodynamics and hydrodynamics of thermal ink jets, *Hewlett-Packard J.* 36 (5) (1985) 21–27.
- [9] P.H. Chen, W.C. Chen, S.H. Chang, Bubble growth and ink ejection process of a thermal ink jet printhead, *Int. J. Mech. Sci.* 39 (6) (1997) 683–689.
- [10] C.T. Avedisian, W.S. Osborne, F.D. McLeod, C.M. Curley, Measuring bubble nucleation temperature on the surface of a rapidly heated thermal ink-jet heater immersed in a pool of water, *Proc. R. Soc. Lond. Ser. A-Math. Phys. Eng. Sci.* 455 (1991) (1999) 3875–3899.
- [11] Y. Suh, G. Son, A level-set method for simulation of a thermal inkjet process, *Numer. Heat Transfer B-Fundam.* 54 (2) (2008) 138–156.
- [12] T. Kraemer, Printing enters the jet age, *Invent. Tech.* 16 (2001) 18–27.
- [13] P.A. Melendez, K.M. Kane, C.S. Ashvar, M. Albrecht, P.A. Smith, Thermal inkjet application in the preparation of oral dosage forms: dispensing of prednisolone solutions and polymorphic characterization by solid-state spectroscopic techniques, *J. Pharm. Sci.* 97 (7) (2008) 2619–2636.
- [14] B.J. de Gans, P.C. Duineveld, U.S. Schubert, Inkjet printing of polymers: state of the art and future developments, *Adv. Mater.* 16 (3) (2004) 203–213.
- [15] B. Derby, Bioprinting: inkjet printing proteins and hybrid cell-containing materials and structures, *J. Mater. Chem.* 18 (47) (2008) 5717–5721.
- [16] T. Xu, J. Rohozinski, W.X. Zhao, E.C. Moorefield, A. Atala, J.J. Yoo, Inkjet-mediated gene transfection into living cells combined with targeted delivery, *Tissue Eng. Part A* 15 (1) (2009) 95–101.
- [17] L. Setti, A. Fraleoni-Morgera, I. Mencarelli, A. Filippini, B. Ballarin, M. Biase, An HRP-based amperometric biosensor fabricated by thermal inkjet printing, *Sens. Actuators B-Chem.* 126 (1) (2007) 252–257.
- [18] C.T. Avedisian, The thermal ink jet printer: a paradigm for microscale phase change, in: *Proceedings of the Fifth ISHMT-ASME Heat and Mass Transfer Conference and Sixteenth National Heat Transfer*, Tata McGraw Hill Publishing Co. LTD., Calcutta, India, 2002, pp. 169–175. ISBN 0-07-047443-5.
- [19] R.E. Cavicchi, C.T. Avedisian, Bubble nucleation, growth and surface temperature oscillations on a rapidly heated microscale surface immersed in a bulk subcooled but locally superheated liquid under partial vacuum, *Int. J. Heat Mass Transfer* 54 (25–26) (2011) 5612–5622.
- [20] R.E. Apfel, water superheated to 279.5 degrees at atmospheric-pressure, *Nat.-Phys. Sci.* 238 (82) (1972) 63–64.
- [21] P.A. Pavlov, V.P. Skripov, Kinetics of spontaneous nucleation in strongly heated liquids, *High Temp.* 8 (3) (1970) 540–545.
- [22] V.P. Skripov, P.A. Pavlov, Explosive boiling of liquids and fluctuation nucleus formation, *High Temp.* 8 (4) (1970) 782–787.
- [23] R.E. Apfel, Vapor cavity formation in liquids, Technical Memorandum no. 62, ed.: Acoustics Research Laboratory, Harvard University, 1970.
- [24] M. Blander, D. Hengstenberg, J.L. Katz, Bubble nucleation in pentane, hexane, pentane and hexadecane mixtures, and water, *J. Phys. Chem.-Us* 75 (23) (1971) 3613–3619.
- [25] C.T. Avedisian, The homogeneous nucleation limits of liquids, *J. Phys. Chem. Ref. Data* 14 (3) (1985) 695–729.
- [26] R.E. Cavicchi, C.T. Avedisian, Bubble nucleation and growth anomaly for a hydrophilic microheater attributed to metastable nanobubbles, *Phys. Rev. Lett.* 98 (2007) 124501.
- [27] C.T. Avedisian, R.E. Cavicchi, M.J. Tarlov, New technique for visualizing microboiling phenomena and its application to water pulse heated by a thin metal film, *Rev. Sci. Instrum.* 77 (6) (2006) 063706.
- [28] K.M. Balss, C.T. Avedisian, R.E. Cavicchi, M.J. Tarlov, Nanosecond imaging of microboiling behavior on pulsed-heated Au films modified with hydrophilic and hydrophobic self-assembled monolayers, *Langmuir* 21 (23) (2005) 10459–10467.
- [29] F.P. Incropera, D.P. DeWitt, *Introduction to Heat Transfer*, fourth ed., Wiley, New York, NY, 2002 (p.824).
- [30] M.J. Carrier, Improvements in microboiling device design (M.S. thesis), Dept. of Materials Science and Engineering, ed.: University of Maryland, College Park, 2011.
- [31] Certain commercial instruments are identified to adequately specify the experimental procedure. In no case does such identification imply endorsement by the National Institute of Standards and Technology.
- [32] J. Lundgren, SPLINEFIT Computer software, MATLAB, ed.: Central. Mathworks, 2007.
- [33] P. Griffith, J.D. Wallis, The role of surface conditions in nucleate boiling, *Chem. Eng. Prog. Symp.* 56 (30) (1960) 49–63.
- [34] Y.S. Qi, J.F. Klausner, Heterogeneous nucleation with artificial cavities, *J. Heat Transfer-T Asme* 127 (11) (2005) 1189–1196.
- [35] V.P. Carey, A.P. Wemhoff, Thermodynamic analysis of near-wall effects on phase stability and homogeneous nucleation during rapid surface heating, *Int. J. Heat Mass Transfer* 48 (2005) 5431–5445.